Available online at www.sciencedirect.com
ScienceDirect
Trans. Nonferrous Met. Soc. China 29(2019) 1383−1392
Transactions of Nonferrous Metals Society of China
www.tnmsc.cn

# Effect of friction stir processing on corrosion of Al−$TiB_2$ based composite in 3.5 wt.% sodium chloride solution

Ritukesh SHARMA[1], Amit Kumar SINGH[2], Amit ARORA[2], S. PATI[1], P. S. DE[1]

1. School of Minerals, Metallurgical and Materials Engineering, Indian Institute of Technology Bhubaneswar, India;
2. Materials Science and Engineering, Indian Institute of Technology Gandhinagar, India

Received 9 October 2018; accepted 14 May 2019

**Abstract:** The microstructure and corrosion behavior of as-cast and friction stir processed in-situ Al−$TiB_2$ based composite in 3.5 wt.% sodium chloride solution were investigated. The microstructure was characterized using X-ray diffractometry, scanning electron microscopy and electron backscattered diffraction technique while corrosion behavior was evaluated using linear/cyclic potentiodynamic, electrochemical impedance spectroscopy and ASTM–G67 tests. The composite contains sub-micron $TiB_2$ particles in an aluminum matrix with both blocky and fine clusters of $Al_3Ti$ agglomerated around $TiB_2$ and displays a low uniform corrosion rate. It is also resistant to pitting as substantiated by the absence of a positive loop in cyclic potentiodynamic tests. This is due to the non-conductive nature of $TiB_2$ particles and a controlled amount of blocky $Al_3Ti$ phase. However, both friction stir processed and as-cast composites are susceptible to inter-granular corrosion where $Al_3Ti$ and $TiB_2$ at grain boundaries provide initiation sites for corrosion. Electrochemical impedance study attributes this to the adverse effect of $Al_3Ti$ and $TiB_2$ on the protective oxide surface film, which increases with immersion time.

**Key words:** friction stir processing; corrosion behavior; Al composite; electrochemical impedance spectroscopy (EIS)

## 1 Introduction

Friction stir welding/processing (FSW/P) is now an established technique to manufacture aluminum alloy components which are difficult to joint using traditional methods [1]. Grain refinement, energy efficiency and avoiding solidification defects such as porosity, liquation cracking, distortion and loss of alloying elements are some of the major benefits making FSW/P a favored technique [2]. The presence of welding procedure standards like ISO 25239-4:2011 further enables manufacturers to take advantage of the process [3]. Nonetheless, methods to improve corrosion resistance and joint efficiency of friction stir welded/processed aluminum alloys continue to attract attention and have led researchers to focus on weldable aluminum-based metal matrix composites (MMCs) due to their reasonable strength, good high-temperature properties, excellent wear [1,3−6] and damping properties [7−9]. Among different aluminum based MMCs, Al−$TiB_2$ based composites exhibit promise in terms of good tensile strength [4], improved elastic modulus, fine particle size, and resistance to brittle layer formation at the matrix−particle interface [5]. Moreover, lack of reaction with aluminum matrix unlike in Al−SiC MMC as well as high electrical resistivity of $TiB_2$ results in improved corrosion properties [5]. Another advantage is the joint efficiency of these composites ranging from ~78% to 100% depending on friction stir processing parameters used [6]. The work on Al−$TiB_2$ based composite and its friction stir welding/processing is focused on the synthesis, mechanical, corrosion and wear properties in the as-cast state [4−6]. The detailed corrosion characteristics of friction stir processed Al−$TiB_2$ based composites are less reported. The present work, therefore, investigates and compares the microstructure and corresponding corrosion properties in an Al−$TiB_2$ based composite for both as-cast and friction stir processed state.

Exhaustive literature exists on corrosion of commercial aluminum alloys [10,11]. A comparative study of the corrosion characteristics of different Al alloys in NaCl solution indicates that commercially pure

**Corresponding author:** P. S. DE; E-mail: parthasarathi.de@iitbbs.ac.in
DOI: 10.1016/S1003-6326(19)65045-4

aluminum has the best corrosion resistance [12,13]. Intermetallics and second phases in aluminum alloys deteriorate the corrosion resistance with matrix−reinforcement interface and areas adjoining grain boundaries acting as preferential sites for corrosion [14]. Thus, in-situ Al−$TiB_2$ composites (stir casting method) in 3.5 wt.% NaCl, 0.5 mol/L $H_2SO_4$ and or 0.5 mol/L NaOH electrolytic solutions have a higher corrosion rate as compared to the base metal [5]. Similarly, in-situ Ti−B dispersed Al matrix composites have a low corrosion resistance [10]. Friction stir welding/processing of a composite will lead to three distinct microstructural regions viz. (1) stir zone, (2) thermo-mechanically affected zone (TMAZ) and (3) heat affected zone (HAZ) with characteristic matrix/reinforcement distribution. This will further alter the corrosion characteristics of an aluminum-based MMC [6,12,15,16].

Thus, inter-granular corrosion occurs at the thermo-mechanically affected zone (TMAZ) in AA 7108-T79 aluminum alloy in 4.0 mol/L NaCl, 0.5 mol/L $KNO_3$ and 0.1 mol/L $HNO_3$ solutions [17]. Similarly, inter-granular and pitting corrosion has been reported for friction stir processed AA 7075 in 3.5 wt.% NaCl solution [18]. On the other hand, the second phase dissolution during FSW/P in AA 2219 improves its pitting corrosion resistance [19]. Thus, the effect of FSW/P on corrosion is principally due to its influence on second phase distribution (i.e., localization or randomization of the phases) as well as its ability to dissolve/re-precipitate the second phases. The second phase particles in as-cast Al−$TiB_2$ based in-situ MMC are fine in size (sub-micron) and distribute principally at the grain boundaries or exist as aggregated clusters within the microstructure. Any alteration in this particle distribution after friction stir processing can result in a considerable change in corrosion characteristics. Therefore, the linear polarization, cyclic polarization and electrochemical impedance characteristics of a friction stir processed Al−$TiB_2$ based composite are measured and compared with those in the as-cast state in more detail.

## 2 Experimental

Test plates of Al−$TiB_2$ MMC with size of 150 mm × 100 mm × 5 mm were prepared by in-situ stir casting process where $K_2TiF_6$ and $KBF_4$ were added into the liquid aluminum melt at ~800 °C and stirred to form $TiB_2$ according to the following reaction [20]:

$$K_2TiF_6(s)+KBF_4(s)+Al(l)\rightarrow TiB_2(s)+AlB_2(l)+Al_3Ti(s)+K_3AlF_6(l)+KAlF_4(l) \quad (1)$$

The schematic diagram in Fig. 1 shows dimensions of the FSW tool used for processing/welding. The cast plate was friction stir processed (FSP) using an H13 steel tool with a shoulder diameter of 18 mm and a probe length of 4.75 mm with a diameter of 7 mm at the root and 3.5 mm at the pin tip. The tilt angle was set at 2° from the vertical axis of the tool and the processing performed with a tool rotation speed of 660 r/min and a traverse speed of 40 mm/min. The microstructures of the cast, as well as the FSP zone, were investigated using optical microscopy, scanning electron microscopy (SEM), and orientation imaging microscopy (OIM) technique. All microscopy samples were prepared using SiC paper and 1 μm diamond paste with the final finish completed using colloidal silica. During the OIM study, identified phases included aluminum and $TiB_2$ with a step size of 0.5 μm used. The grain size and phase fractions were calculated using ImageJ software [21].

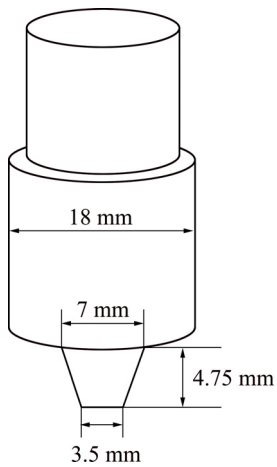


**Fig. 1** Schematic diagram of friction stir welding tool used in this work

The linear polarization experiments on the FSP and as-cast MMC were conducted at room temperature in a typical three-electrode cell setup (flat cell) with the specimen as working electrode, saturated calomel electrode (SCE) as the reference and a standard platinum as counter electrode. A sodium chloride (NaCl) solution (3.5 wt.%) purged using nitrogen was used as the electrolyte. The applied potential ranged from −250 to +250 mV (ASTM G5) with respect to the stabilized open circuit potential ($\varphi_{ocp}$) at a voltage scan rate of 0.6 V/h. The polarization samples for as-cast composite were diamond polished (3−4 μm), washed with detergent and dried in ethanol before conducting the experiments. For the FSP composite, the tool shoulder affected region was polished and used. The pitting corrosion susceptibility was investigated using cyclic polarization technique where cyclic scan consisting of one full cycle starting from $\varphi_{ocp}$ to +0.5 V with a reversion to −0.5 V, followed by a return to $\varphi_{ocp}$ at a rate of 0.6 V/h was employed.

The inter-granular corrosion (IGC) propensities for both as-cast and FSP samples were ascertained using the

ASTM G67 standard. The inter-granular corrosion test specimens (18 mm × 18 mm × 3mm) were prepared as follows: (1) Etching the samples in 5% NaOH solution at 80 °C for 1 min; (2) Desmutting in 70% $HNO_3$ for 30 s. The prepared specimens were immersed in 70% $HNO_3$ at room temperature for 24 h followed by measurements of the mass lost per unit area to determine the inter-granular corrosion susceptibility (NAMLT-test) [22]. Subsequently, the inter-granular corrosion extent in sectioned and polished specimens (after corrosion) was microscopically determined.

For Electrochemical impedance spectroscopy (EIS) tests, both samples were diamond polished (3−4 μm) and the spectrum was obtained using a potentiostat coupled to a frequency response analyzer. The amplitude of the AC signal applied was ±10 mV with frequency ranging from $10^5$ to 0.1 Hz at OCP. The final equivalent circuit for the electrochemical response was simulated using Autolab NOVA software.

## 3 Results

### 3.1 Microstructure and phases

The high magnification secondary electron (SE) image of the as-cast composite presented in Fig. 2 reveals dispersed $TiB_2$ particles as well as $Al_3Ti$−$TiB_2$ agglomerates and is similar to that reported by TEE et al [4]. In Figs. 3(a) and (c), the composition mode back-scattered electron (BS) images of the as-cast and FSP sample display grain boundary $TiB_2$ precipitates and flaky $Al_3Ti$ akin to that observed by TEE et al [4] and WANG et al [20].

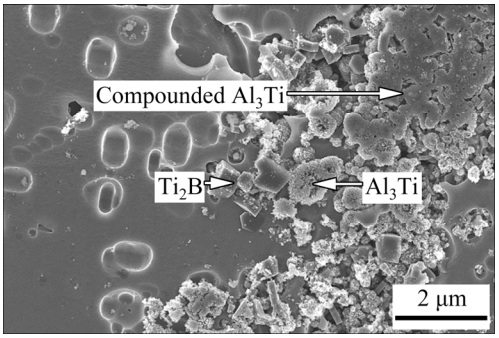


**Fig. 2** Secondary electron image of as-cast sample

In Figs. 3(b) and (d), the OIM images of the as-cast and FSP specimen with both $TiB_2$ particles (result of in-situ reaction) and unresolved regions of the microstructure are presented. The unresolved region is an outcome of overlapping patterns from multiple phases like $Al_3Ti$, $TiB_2$ and aluminum. Both as-cast and FSP microstructures exhibit high angle and low angle grain boundaries with the low angle boundaries located preferentially near the second phases (Figs. 3(b) and (d)). Figure 4 exhibits the energy dispersive spectroscopy (EDS) composition map depicting aluminum, titanium and boron distribution in the FSP sample. The X-ray diffraction (XRD) pattern of the composite (Fig. 5) also

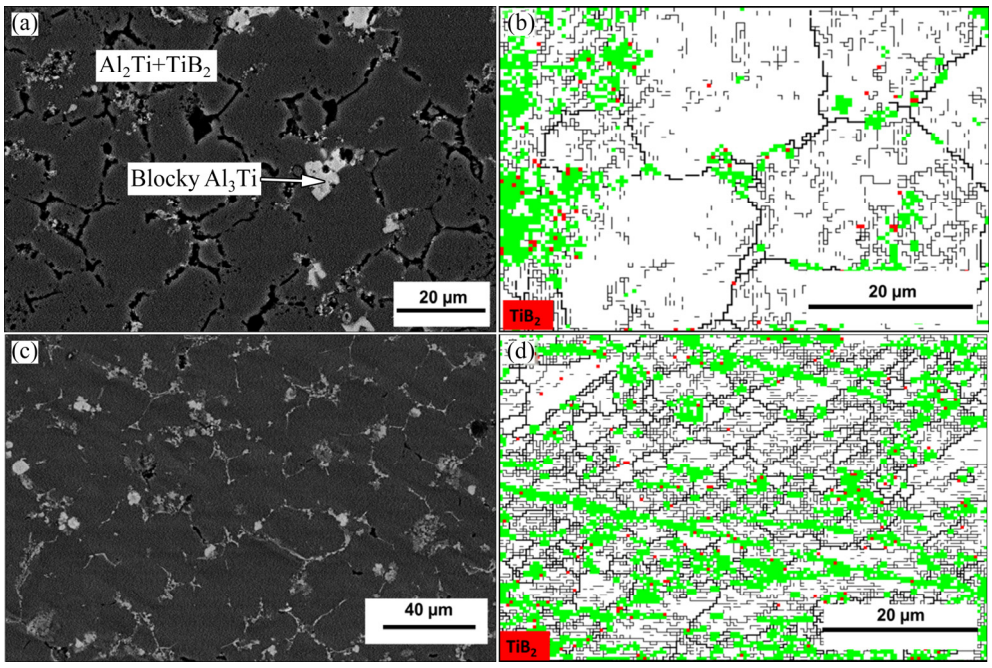


**Fig. 3** SEM microstructures of Al−$TiB_2$ composite: (a) Compositional mode back-scattered image of as-cast specimen; (b) OIM image of as-cast specimen; (c) Compositional mode back-scattered image of FSP specimen; (d) OIM image of FSP specimen (The thick dark black lines in OIM image represent high angle grain boundaries and thin black lines represent low angle grain boundaries; Two phases, i.e., $TiB_2$ and aluminum, are identifiable in the FSP sample while the green region is the unresolved phase; In the OIM images, the $Al_3Ti$ phase is not shown)

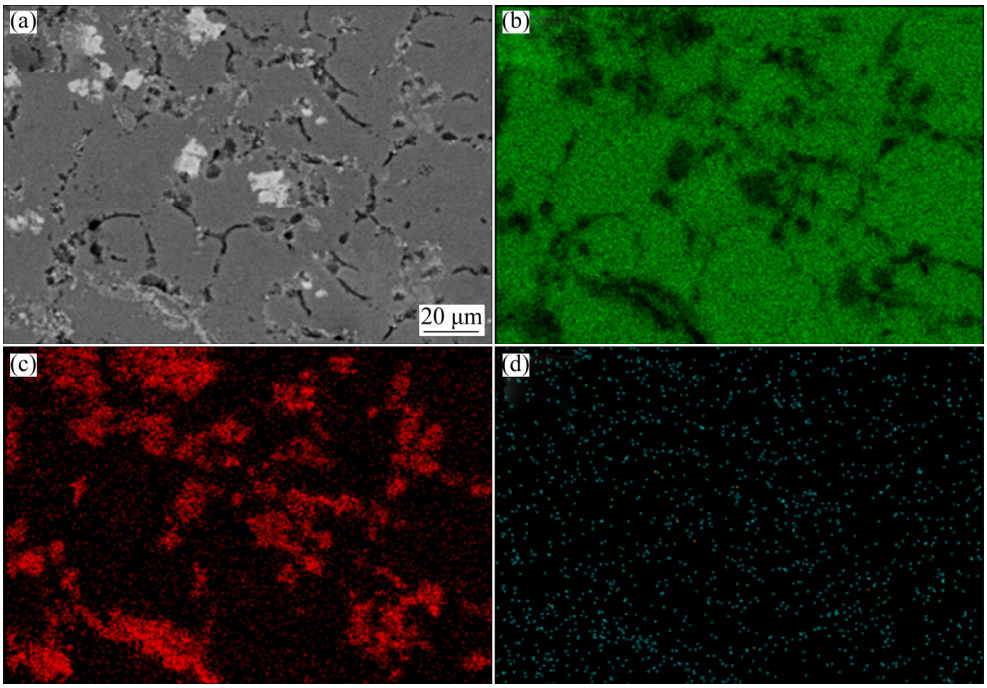


**Fig. 4** Energy dispersive spectroscopy mapping of friction stir processed Al−$TiB_2$ composite: (a) Electron image; (b) Al; (c) Ti; (d) B

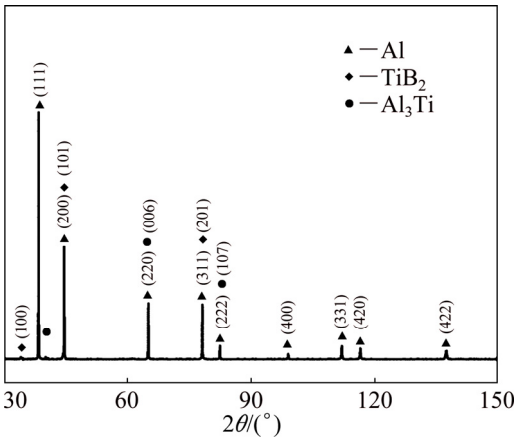


**Fig. 5** Powder X-ray diffraction pattern of as-cast Al−$TiB_2$ composite

confirms these three phases identified in the SEM image. Using Klug and Alexander method, the volume fractions of $TiB_2$ in the as-cast and FSP composites are estimated to be ~5% and ~4%, respectively [23]. ImageJ analysis of as-cast composite microstructure reveals that the volume fraction of the blocky $Al_3Ti$ phase is (3.5±0.5)% and (5.7±1.4)% for the phase clustered with $TiB_2$. For the FSP specimen, the volume fraction obtained is (2.1±0.6)% (blocky) and (6.3±1.7)% (clustered with $TiB_2$), respectively.

The grain size of the FSP Al−$TiB_2$ composite obtained from OIM analysis is (5.3±2.3) μm as compared to (16.8±2.4) μm for as-cast composite obtained from optical images. The bulk hardness across the FSP zone is (65±2) HV and is similar to base alloy hardness of (61±1) HV.

### 3.2 Corrosion

The resistance polarization as determined by a linear fit of $\Delta\varphi/\Delta J$ for FSP and the as-cast alloy is (10.2±2.2) and (3.9±1.2) kΩ, respectively. The corrosion current density ($J_{corr}$) is subsequently calculated using the relation [24]:

$$J_{corr} = \frac{\alpha\beta}{2.3R(\alpha+\beta)} \tag{2}$$

where $\alpha$ and $\beta$ are the anodic and cathodic Tafel constants (V/dec) of current, and $R$ is the resistance polarization. The linear slope of anodic and cathodic parts (i.e., $\alpha$ and $\beta$) of the linear polarization curve (Fig. 6) are obtained as (0.031±0.002) and (0.325±0.02) V/dec for FSP composite and (0.019±0.003) and (0.462±0.02) V/dec for the as-cast composite. In Table 1, the $\varphi_{corr}$ and $J_{corr}$ values for FSP and as-cast composite, as well as corrosion rate (i.e., penetration rate), are obtained using the following equation [24]:

$$R_C = \frac{0.00327 J_{corr} \cdot e}{d} \tag{3}$$

where a density $d$ of 2.75 gm/cm$^3$ and an equivalent mass $e$ of 9.22 are used.

In Fig. 7, the cyclic polarization curves for both the samples indicate the extent of pitting corrosion and the protection potential ($\varphi_{proc}$) (for values see Table 2). In both cases, i.e., as-cast and FSP, no positive hysteresis

loop or a sudden increase in corrosion current is observed. The results of the inter-granular corrosion test with the mass of the samples before and after exposure to 70% $HNO_3$ are stated in Table 3.

In Fig. 8, the secondary electron image of the FSP cross section after the inter-granular corrosion test is

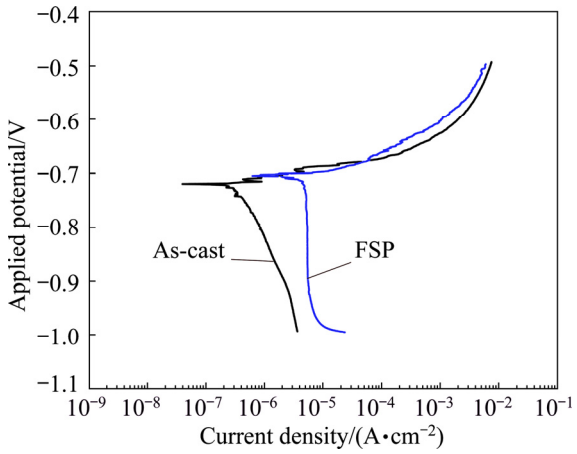


**Fig. 6** Typical Tafel plots for FSP and as-cast Al−$TiB_2$ based composites

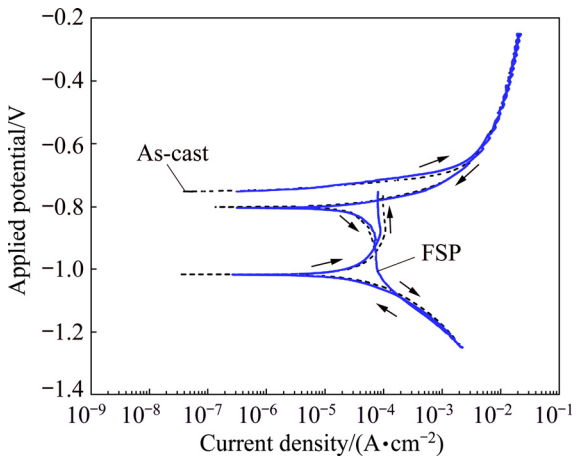


**Fig. 7** Typical cyclic polarization curves of FSP and as-cast Al−$TiB_2$ based composite (Both curves display the absence of a positive hysteresis loop)

**Table 1** Linear potentiodynamic test results for FSP and as-cast composites in 3.5 wt.% NaCl solution

| Composite | Corrosion potential, $\varphi_{corr}$/mV | Corrosion current density, $J_{corr}$/(μA·cm$^{-2}$) | Corrosion rate, $R_C$/(mm·a$^{-1}$) |
|---|---|---|---|
| As-cast | −745.93±9.45 | 2.03±0.30 | 0.022±0.004 |
| FSP | −745.57±4.71 | 1.30±0.20 | 0.014±0.003 |

**Table 2** Cyclic polarization results in 3.5 wt.% NaCl solution

| Sample | $\varphi_{corr}$/mV | $\varphi_{proc}$/mV |
|---|---|---|
| As-cast | −745.93±9.45 | −787.81±5.16 |
| FSP | −745.57±4.71 | −803.10±3.21 |

**Table 3** Inter-granular corrosion test results for given composite

| Sample | Sample mass before exposure/mg | Sample mass after exposure/mg | Mass loss rate/(mg·cm$^{-2}$) |
|---|---|---|---|
| As-cast | 2.8±0.1 | 2.6±0.1 | 42.6±3.9 |
| FSP | 2.4±0.1 | 2.3±0.1 | 37.7±1.8 |

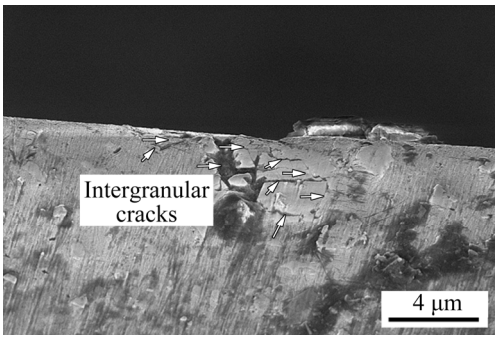


**Fig. 8** Secondary electron image of cross-section of FSP sample after inter-granular corrosion (IGC) test

presented. In Fig. 9(a), the Nyquist plot for the as-cast and FSP sample after 12 and 72 h of immersion in 3.5 wt.% NaCl solution is shown. The equivalent circuit simulating the response of the as-cast and FSP sample after 12 and 72 h of immersion is depicted in Fig. 9(b). The circuit consists of a parallel resistor−capacitor arrangement in series with the solution resistance, $R_s$, where a constant phase element (CPE), instead of capacitance $C$ is used. The impedance of the equivalent circuit is given as [25,26]

$$Z = R_s + \frac{R_p}{1+(j\omega)^n R_p Q} \tag{4}$$

where $R_p$ is the polarization resistance while $Q$ and $n$ correspond to constant phase element (CPE) parameters; $j^2=-1$ and $0\le n\le 1$ [27]. For $n$=1, CPE represents a purely capacitive behavior, while $n$=0 and $n$=0.5 signify a resistor and Warburg impedance, respectively [27]. The element values for the equivalent circuit of spectra after 12 h of immersion are given in Table 4. The Bode magnitude and phase plots for different hours of immersion are shown in Figs. 9(c) and (d).

## 4 Discussion

### 4.1 Microstructure and hardness

For the given composite, segregation and clustering of $TiB_2$ particles occur during solidification leading to inter-granular distribution (Figure 3(a)) and are attributed to [28−30]:

(1) High interfacial energy between Al and $TiB_2$.

(2) Lower interface velocity than the critical velocity ($V_c$) leading to rejection of $TiB_2$ particles towards

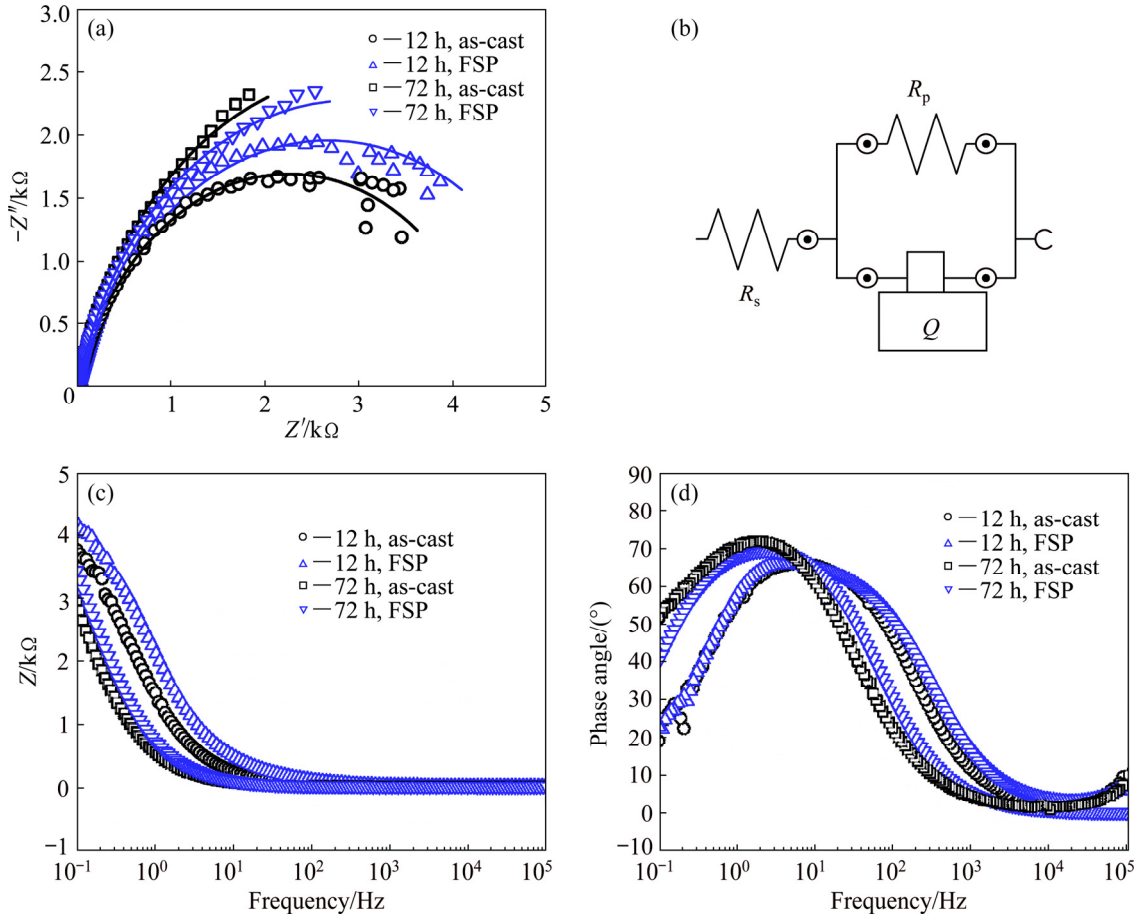


**Fig. 9** Nyquist plots (a), equivalent circuit (b), Bode magnitude plots (c) and Bode phase plot (d) of as-cast and FSP samples after 12 and 72 h of immersion

**Table 4** Element values of equivalent circuit after 12 h of immersion

| Composite | $R_s$/ ($\Omega\cdot cm^2$) | $R_p$/ ($k\Omega\cdot cm^2$) | $Q$/ ($\mu F\cdot cm^{-2}$) | $n$ |
|---|---|---|---|---|
| As-cast | 21.7±1.5 | 5.1±1.3 | 130±11.2 | 0.86±0.04 |
| FSP | 19.8±1 | 5.9±1.3 | 117±20.7 | 0.86±0.06 |

the grain boundaries [31]:

$$V_c^2 = \frac{4kT\gamma a_o \alpha(1-\alpha)^3}{9\pi\eta^2 R^3(1-3\alpha)} \quad (5)$$

where $\eta$ is the viscosity of the liquid, $T$ is temperature, $\gamma$ is the free energy of solid/liquid interface, $R$ is the radius of the particle, $a_o$ is the distance between particle and solid/liquid interface, $k$ is the curvature of the solid/liquid interface and $\alpha$ is the ratio of particle radius to interface radius.

(3) The longer cooling time of in-situ composite melt compared to conventional stir cast composites. This is due to an exothermic reaction extending through some duration of solidification causing the solidification front to sustain longer.

Although several methods to reduce particle clustering are available [32−34], the FSP/FSW holds special promise due to its ability to change the particle distribution locally under solid state conditions. During FSP, large local plastic deformation from retreating to the advancing side results in a more uniform distribution of $TiB_2$ particles [35]. Concurrent, dynamic recrystallization during FSP results in a fine grain size of ~3 μm [30] and is similar to the grain size produced in this work. The reported strengthening from ~38 (as-cast) to ~51 HV by YADAV BAURI [30] differs from the insignificant hardness improvement in the present work (by ~5 HV). This variation is primarily due to the finer initial as-cast grain size in present work (~17 μm) and the additionally dispersed $Al_3Ti$ phase resulting in further grain refinement and strengthening of matrix [20]. It may be mentioned that formation reaction for the $Al_3Ti$ phase is an exothermic process and is favored at low temperatures [4] where $TiB_2$ particles react with the aluminum melt to form a solid solution of $(Ti,Al)B_2$. This solid solution combines with titanium to form $Al_3Ti$ particles where $TiB_2$ particles act as a substrate for nucleation [20]. The above phenomenon is evident in Fig. 3(a) where smaller $Al_3Ti$ particles (indicated by arrow) nucleate on the surface of $TiB_2$ particles with $TiB_2$

particles at its core. As indicated by the arrow in Fig. 2, the large $Al_3Ti$ flakes are compounded particles composed of $TiB_2$ embedded within the $Al_3Ti$ particles. These large $Al_3Ti$ flakes are agglomerates of smaller $Al_3Ti$ particles and push a large number of $TiB_2$ particles to the grain boundaries with some buried inside the compounded $Al_3Ti$ (see Fig. 2). Similar growth of $Al_3Ti$ phase is absent in the work of YADAV and BAURI [30] or in the AA 7075−$TiB_2$ composite reported by RAJAN et al [29]. This difference in phase constituents between the present work and Refs. [29,30], i.e., the absence of $Al_3Ti$, is probably due to the reduced processing temperature of 800 °C (by ~50 °C) used in this work.

### 4.2 Uniform corrosion

The corrosion resistance of commercially pure aluminum is better than that of most of the available aluminum alloys, primarily due to a tenacious oxide layer formed at its surface [36]. Alloying additions in aluminum and consequent secondary phases formed degrade the oxide layer and reduce the corrosion resistance. A similar decrease in corrosion resistance is observed in aluminum-based composites (Table 5) and is influenced by [29] (1) length of reinforcement which acts as a cathode, (2) presence of interfacial phases with high corrosion rates and (3) matrix defects acting as sites for corrosion.

Expectedly, in the present study, both friction stir welded and as-cast composites have inferior $\varphi_{corr}$ and $J_{corr}$ values compared to commercially pure aluminum (Table 5). This lower corrosion resistance of Al−$TiB_2$ composite is due to Al/$TiB_2$ interface acting as initiation sites for corrosion [10].

Quite significantly, $J_{corr}$ for as cast and processed Al−$TiB_2$ in this work is lower compared to aluminum−boron composite (Al−B). On the other hand, the results are similar to Al−SiC composite in Ref. [37] but lower compared to PARDO et al [38] and MOSLEH-SHIRAZI et al [39] (refer to Table 5). In Al−B composites, imperfect bonding and fissures at the Al/B interface as well as intermetallics present cause accelerated corrosion [36]. Similarly, crevices formed at the Al/SiC interface are the primary cause of corrosion in Al−SiC composites [36]. Thus, considering the corrosion rate, the Al−$TiB_2$ composite in the present study is superior to Al−SiC and Al−B composites reported in the literature. The corrosion current density of the aluminum−graphite (Al−G) based composites is much higher than all other Al-based MMCs [40].

Another point to note is the significantly lower $J_{corr}$ value for the composite investigated in the present study compared to that reported in the literature. HUO and TJONG [41] measured the $J_{corr}$ value in Al−2.8%$TiB_2$ and 11.7% $Al_3Ti$ composite as 12.39 μA/cm$^2$ which is ~6 times larger than that of as-cast and ~10 times larger than that of the friction stir processed composite in this work. In fact, the $J_{corr}$ value of ~8.79 μA/cm$^2$ reported for Al−8.7%$TiB_2$ composite [41] is also significantly higher than that of the composite under the present consideration. One major difference between the composite studied in this work and by HUO and TJONG [41] is in the volume fraction and distribution of $Al_3Ti$. The $Al_3Ti$ phase is both conductive and noble with respect to the matrix and increases the susceptibility of Al−$TiB_2$ composites to corrosion [41]. In the present work, the $Al_3Ti$ phase morphology is a combination of blocks (~3%) and clusters with $TiB_2$ (~6%) where clusters are sub-micron in size. The smaller $Al_3Ti$ clusters in the present work eliminate the defects formed on the passive films giving better resistance to corrosion unlike those in Ref. [41].

**Table 5** Comparison of present material with aluminum and Al-based composites

| Material | Corrosion potential, $\varphi_{corr}$/ mV | Corrosion current, $J_{corr}$/ (μA·cm$^{-2}$) | Corrosion rate, $R_C$/ (mm·a$^{-1}$) |
|---|---|---|---|
| As-received aluminum [12] | −843 | 0.89 | 0.0101 |
| Al with dispersed $TiB_2$ [12] | −736 | 2.30 | 0.027 |
| 2024Al−18vol.%B [43] | −775 | 5.00 | 0.053 |
| 2024Al−33vol.%B | −755 | 6.60 | 0.071 |
| 2024Al−46vol.%B | −745 | 9.00 | 0.099 |
| Al−1%G [39]* | −1260 | 155 | 0.760 |
| Al−2%G [39]* | −1270 | 255 | 1.040 |
| Al−3%G [39]* | −1300 | 481 | 1.850 |
| 6061Al−SiC [37] | −732 | 1.50 | 0.015 |
| Al−5wt.%SiC [38] | −785.6 | 133.8 | 1.397 |
| Al−15wt.%SiC [38] | −792.6 | 158.3 | 1.633 |
| Al−25wt.%SiC [38] | −777.8 | 442.3 | 4.536 |
| Al−35wt.%SiC [38] | −786.1 | 168.3 | 1.719 |
| Al 6061−1wt.%SiC [39] | −580 | 13 | 0.17 |
| Al 6061−2wt.%SiC [39] | −577 | 8.4 | 0.13 |
| Al 6061−3wt.%SiC [39] | −571 | 3.9 | 0.03 |

*—Al−graphite composites after 40 min immersion

### 4.3 Pitting and inter-granular corrosion resistance

Susceptibility of metal to pitting corrosion results in high anodic current density during the return scan of cyclic polarization test as compared to the forward scan at a given anodic potential [42]. Such 'positive hysteresis' behavior is absent in the present work (Fig. 7) and rationalizes the absence of pitting in both the as-cast and FSP specimens. This behavior of Al−$TiB_2$ composite

is in variation with that reported earlier [10].

The presence of a high volume fraction of intermetallics promotes galvanic effect and causes pitting in most of the composites. Thus, in Al−B composites, an increased localized attack occurs due to the galvanic coupling between the matrix and Al−B intermetallic compounds [43]. In Al−SiC composites, the large potential difference between Al and SiC provides a driving force for pitting corrosion leading to crevice formation [44]. The corrosion rate further increases due to intermetallics formed in Al−SiC composites [44]. Similarly, the clustering of reinforcement and high intermetallic volume fraction provide a large cathodic area in aluminum−alumina (Al−$Al_2O_3$) and aluminum−titanium carbide (Al−TiC) composites [45,46] causing susceptibility to pitting.

On the contrary, in Al−$TiB_2$ composite, $TiB_2$ on the exposed surface forms an oxide layer of $TiO_2 \cdot H_2O$ after immersion in ocean water solution at room temperature [47]. This along with the covalent character of $TiB_2$ results in minimum galvanic effect between Al and $TiB_2$. Further, as discussed in Section 4.2, the homogenous distribution of $Al_3Ti$ phase within the matrix and its small size reduce the galvanic effect at Al/$Al_3Ti$ interfaces. Friction stir processing further disperses the $Al_3Ti$ and the pitting resistance remains unaffected.

However, mass loss test (see Table 3) occurring on exposure to $HNO_3$, (greater than 25 mg/cm$^2$) and corresponding high magnification image of the corroded region indicate inter-granular corrosion (indicated by white arrows in Fig. 8) [22]. The FSP region is slightly less prone compared to as-cast composite (see Table 3). To understand this IGC behavior, the principal factors governing inter-granular corrosion in Al alloys are given below [48,49]:

(1) Corrosion potential difference between grain boundary precipitate and matrix.

(2) Differences in breakdown potential between solute depleted zone and matrix.

(3) Dissolution of grain boundary phases leading to continuous grain boundary attack.

In fact, friction stir processing of non-heat-treatable AA 5083 alloy reduces its inter-granular corrosion susceptibility due to fine grain size and homogenous distribution of precipitates [50]. OGUOCHA et al [51] explained that low angle grain boundaries are less susceptible to IGC than their high angle counterparts. High angle boundaries possess high grain boundary energy and are of incoherent type compared to a coherent low angle grain boundary [52]. Thus, grain boundary precipitates form preferentially at high angle grain boundaries leading to high IGC susceptibility [52]. In fact, OIM image of the as-cast and FSP Al−$TiB_2$ composite (Figs. 3(b) and (d)) indicates a uniform distribution of $TiB_2$ particles mostly along the high angle grain boundaries. Moreover, a large amount of plastic deformation during FSP/FSW results in fine recrystallized grains [35] with the concentration of low angle boundary being higher in FSP specimen compared to the as-cast structure (Figs. 3(b) and (d)). Such an increase in low angle grain boundaries leads to more active oxidation sites and extensive surface film formation and decreases the IGC susceptibility of the FSP sample [53]. Thus, the difference in IGC susceptibility between FSP Al−$TiB_2$ and the as-cast sample is primarily due to (1) fine recrystallized grains with high low angle boundary concentration and (2) reduction in corrosion initiation sites at the grain boundary.

### 4.4 Electrochemical impedance measurement

The Nyquist plot (Fig. 9(a)) for both the FSP and as-cast samples shows only one capacitive contribution represented by a semicircle. Bode phase plot (Fig. 9(d)) indicates the presence of a single time constant at low frequency. The impedance responses are resistive at high frequency as indicated by practically no phase shifts whereas at a low frequency they are mostly capacitive and the phase shift gets closer to 90° (Fig. 9(d)). The diameters of the capacitance arcs decrease with an increase in immersion time. The increase of $R_p$ value with immersion time indicates good corrosion resistance while a high value of CPE indicates lower stability of the protective passive film on the composite [54]. The $R_p$ values for both the as-cast and FSP samples after 72 h of immersion (~6 kΩ·cm$^2$ for both) do not vary significantly from those after 12 h (see Table 4). However, as compared to 12 h specimens (see Table 4), the CPE value increases after 72 h of immersion ($Q$ values are about 380 and 280 μF/cm$^2$ for as-cast and FSP samples, respectively), resulting in lower absolute impedance for both the samples (Fig. 9(c)). Based on these results, it may be deduced that the distribution of $Al_3Ti$ and $TiB_2$ particles affects the protection of surface film with immersion time in both as-cast and FSP composites as indicated by an increase in $Q$ values and explains the susceptibility of the composites to IGC after 24 h of immersion.

## 5 Conclusions

(1) The composite processed at 800 °C contains three principal phases: Al, $Al_3Ti$ and $TiB_2$.

(2) The Al−$TiB_2$ composite (as-cast and friction stir processed) exhibits much better corrosion resistance compared to Al−B and Al−graphite and is comparable to Al−SiC based composites.

(3) Both friction stir processed and the as-cast Al−$TiB_2$ based composite resists pitting corrosion in contrast to Al−B, Al−G and Al−SiC composites.

(4) The friction stir processed sample is less prone to inter-granular corrosion than the as-cast composite due to finer grain size and a higher fraction of low angle grain boundaries.

(5) The electrochemical impedance study indicates that $TiB_2$ and $Al_3Ti$ particles reduce the protective effect of the surface film with increasing immersion time resulting in intergranular corrosion.

## Acknowledgments

During experiments, the assistance of Mr. Sidhant Pathak, Mr. Tadisetty Sivaji, Mr. Ananta Dutta, Master's students, Mr. Uttam Kumar Chanda, Ph.D student, at IIT Bhubaneswar and Mr. Loknath, scientific assistant in SEM laboratory IIT Bhubaneswar is greatly appreciated. Some of the authors (Amit Kumar SINGH and Amit ARORA) would like to acknowledge the financial support from the Board for Research in Nuclear Sciences (BRNS) (Project number 36(2)/20/02/2014-BRNS/).

## References

[1] DE P S, MISHRA R S. Friction stir welding of precipitation strengthened aluminum alloys: Scope and challenges [J]. Science and Technology of Welding and Joining, 2011, 16(4): 343−347.

[2] NANDAN R, DEBROY T, BHADESHIA H. Recent advances in friction-stir welding−Process, weldment structure and properties [J]. Progress in Materials Science, 2008, 53(6): 980−1023.

[3] MISHRA R S, DE P S, KUMAR N. Friction stir welding and processing [M]. Springer, 2014.

[4] TEE K L, LU L, LAI M O. In situ stir cast Al−$TiB_2$ composite: Processing and mechanical properties [J]. Materials Science and Technology, 2001, 17(2): 201−206.

[5] SEKHAWAT D S, CHAKRABORTY M, CHATTERJEE U K. Wear and corrosion behaviour of in-situ Al−$TiB_2$ metal matrix composites [J]. Materials Science Forum, 2005, 475−479: 449−452.

[6] VIJAY S J, MURUGAN N. Influence of tool pin profile on the metallurgical and mechanical properties of friction stir welded Al−10wt.%$TiB_2$ metal matrix composite [J]. Materials Design, 2010, 31(7): 3585−3589.

[7] NI D R, WANG J J, MA Z Y. Shape memory effect, thermal expansion and damping property of friction stir processed $NiTi_p$/Al composite [J]. Journal of Materials Science and Technology, 2016, 32(2): 162−166.

[8] SRIKANTH N, CALVIN H, GUPTA M. Effect of length scale of alumina particles of different sizes on the damping characteristics of an Al−Mg alloy [J]. Materials Science and Engineering A, 2006, 423(1−2): 189−191.

[9] MADEIRA S, MIRANDA G, CARNEIRO V H, SOARES D, SILVA F S, CARVALHO O. The effect of $SiC_p$ size on high temperature damping capacity and dynamic Young's modulus of hot-pressed AlSi−$SiC_p$ MMCs [J]. Materials Design, 2016, 93: 409−417.

[10] VARGEL C, JACQUES M, SCHMIDT M P. Corrosion of aluminium [M]. Elsevier, 2004.

[11] DAVIS J R. Corrosion of aluminum and aluminum alloys [M]. Materials Park, Ohio, USA: ASM International, 1999.

[12] MAJUMDAR J D, CHANDRA B R, NATH A K, MANNA I. In situ dispersion of titanium boride on aluminium by laser composite surfacing for improved wear resistance [J]. Surface Coating Technology, 2006, 201(3−4): 1236−1242.

[13] TRUEBA M, TRASATTI S P. Study of Al alloy corrosion in neutral NaCl by the pitting scan technique [J]. Material Chemistry and Physics, 2010, 121(3): 523−533.

[14] RAMGOPAL T, GOUMA P I, FRANKEL G S. Role of grain-boundary precipitates and solute-depleted zone on the intergranular corrosion of aluminum alloy 7150 [J]. Corrosion Science, 2002, 58(8): 687−697.

[15] UZUN H. Friction stir welding of SiC particulate reinforced AA2124 aluminium alloy matrix composite [J]. Materials Design, 2007, 28(5): 1440−1446.

[16] MISHRA R S, MA Z Y, CHARIT I. Friction stir processing: A novel technique for fabrication of surface composite [J]. Materials Science and Engineering A, 2003, 341(1−2): 307−310.

[17] WADESON D A, ZHOU X, THOMPSON G E. Corrosion behaviour of friction stir welded AA7108 T79 aluminium alloy [J]. Corrosion Science, 2006, 48(4): 887−897.

[18] NAVASER M, ATAPOUR M. Effect of friction stir processing on pitting corrosion and intergranular attack of 7075 aluminum alloy [J]. Journal of Materials Science and Technology, 2017, 33(2): 155−165.

[19] SUREKHA K, MURTY B S, RAO K P. Comparison of corrosion behaviour of friction stir processed and laser melted AA 2219 aluminium alloy [J]. Materials Design, 2011, 32(8−9): 4502−4508.

[20] WANG X, SONG J, VIAN W, MA H, HAN Q. The interface of $TiB_2$ and $Al_3Ti$ in molten aluminum [J]. Metallurgical and Materials Transaction B, 2016, 47(6): 3285−3290.

[21] SCHNEIDER C A, RASBAND W S, ELICEIRI K W. NIH Image to ImageJ: 25 years of image analysis [J]. Nature Methods, 2012, 9(7): 671−675.

[22] Test method for determining the susceptibility to intergranular corrosion of 5XXX series aluminum alloys by mass loss after exposure to nitric acid (NAMLT Test) [S]. ASTM International, 2004.

[23] NORRISH K, TAYLOR R M. Quantitative analysis by X-ray diffraction [J]. Clay Miner Bulletin, 1962, 5(28): 98−109.

[24] MANSFELD F. Corrosion: Fundamentals, testing, and protection [J]. ASM International A, 2003, 13: 446−462.

[25] ISMAIL K M, EL-EGAMY S S, ABDELFATAH M. Effects of Zn and Pb as alloying elements on the electrochemical behaviour of brass in borate solutions [J]. Journal of Applied Electrochemistry, 2001, 31(6): 663−670.

[26] TRDAN U, GRUM J. Evaluation of corrosion resistance of AA6082-T651 aluminium alloy after laser shock peening by means of cyclic polarisation and EIS methods [J]. Corrosion Science, 2012, 59: 324−333.

[27] MACDONALD J R, BARSOUKOV E. Impedance spectroscopy: Theory, experiment, and applications [M]. 2nd ed. New York: Wiley-Interscience, 2005.

[28] YOUSSEF Y M, DASHWOOD R J, LEE P D. Effect of clustering on particle pushing and solidification behaviour in $TiB_2$ reinforced aluminium PMMCs [J]. Composites, 2005, 36(6): 747−763.

[29] RAJAN H, DINAHARAN I, RAMABALAN S, AKINLABI E T. Influence of friction stir processing on microstructure and properties of AA7075/$TiB_2$ in situ composite [J]. Journal of Alloys and Compounds, 2016, 657: 250−260.

[30] YADAV D, BAURI R. Friction stir processing of Al−$TiB_2$ in situ composite: Effect on particle distribution, microstructure and properties [J]. Journal of Materials Engineering and Performance, 2015, 24(3): 1116−1124.

[31] CHAWALA N, CHAWALA K K. Metal matrix composites [M]. 2nd ed. Springer, 2006.

[32] WATSON I G, FORSTER M F, LEE P D, DASHWOOD R J, HAMILTON R W, CHIRAZI A. Investigation of the clustering behaviour of titanium diboride particles in aluminium [J]. Composites, 2005, 36 (9): 1177−1187.

[33] SOLTANI N, JAFARI NODOOSHAN H R, BAHHRAMI A,

PECH-CANUL M I, LIU WU W G. Effect of hot extrusion on wear properties of Al−15wt.%$Mg_2Si$ in situ metal matrix composites [J]. Materials Design, 2014, 53: 774−781.

[34] HERBERT M A, MAITI R, MITRA R, CHAKRABORTY M. Wear behaviour of cast and mushy state rolled Al−4.5Cu alloy and in-situ Al4.5Cu−5$TiB_2$ composite [J]. Wear, 2008, 265(11−12): 1606−1618.

[35] MISHRA R S, MA Z Y. Friction stir welding and processing [J]. Materials Science and Engineering R, 2005, 50(1−2): 1−78.

[36] SNODGRASS J, MORAN J. Corrosion: Fundamentals, Testing, and Protection, ASM handbook 13A [M]. Materials Park, Ohio, USA: ASM International, 2003.

[37] NEIL W, GARRARD C. The corrosion behaviour of aluminium−silicon carbide composites in aerated 3.5% sodium chloride [J]. Corrosion Science, 1994, 36(5): 837−851.

[38] PARDO A, MERINO M C, MERINO S, VIEJO F, CARBONERAS M, ARRABAL R. Influence of reinforcement proportion and matrix composition on pitting corrosion behaviour of cast aluminium matrix composites (A3xx.x/$SiC_p$) [J]. Corrosion Science, 2005, 47(7): 1750−1764.

[39] MOSLEH-SHIRAZI S, AKHLAGHI F, LI Dong-yang. Effect of SiC content on dry sliding wear, corrosion and corrosive wear of Al/SiC nanocomposites [J]. Transactions of Nonferrous Metals Society of China, 2016, 26: 1801−1808.

[40] EL-SAYED S M, ALMAJIDl A A, LATIF F H. Effects of graphite on the corrosion behavior of aluminum−graphite composite in sodium chloride solutions [J]. International Journal of Electrochemical Science, 2011, 6: 1085−1099.

[41] HUO H, TJONG S C. Corrosion behavior of Al-based composites containing in-situ $TiB_2$, $Al_2O_3$ and $Al_3Ti$ reinforcements in aerated 3.5% sodium chloride solution [J]. Advanced Engineering Materials, 2007, 9(7): 588−593.

[42] CHOU Y L, YEH J W, SHIH H C. The effect of molybdenum on the corrosion behaviour of the high-entropy alloys Co1.5CrFeNi1.5-Ti0.5Mo*x* in aqueous environments [J]. Corrosion Science, 2010, 52(8): 2571−2581.

[43] POHLMAN S L. Corrosion and electrochemical behavior of boron/aluminum composites [J]. Corrosion, 1978, 34(5): 156−159.

[44] GURRAPPA I, PRASAD V B. Corrosion characteristics of aluminium based metal matrix composites [J]. Materials Science and Technology, 2006, 22(1): 115−122.

[45] de SALAZAR J M G, URENA A, MANZANEDO S, BARRENA M I. Corrosion behaviour of AA6061 and AA7005 reinforced with $Al_2O_3$ particles in aerated 3.5% chloride solutions: Potentiodynamic measurements and microstructure evaluation [J]. Corrosion Science, 1998, 41(3): 529−545.

[46] SARAVANAN S, SENTHILKUMAR P, RAVICHANDRAN M, ANANDAKRISHNAN V. Mechanical, electrical, and corrosion behavior of AA6063/TiC composites synthesized via stir casting route [J]. Journal of Materials Research, 2017, 32(3): 606−614.

[47] COVINO B S, CRAMER S D, CARTER J P, SCHLAIN D. Corrosion of titanium diboride [J]. Journal of Less-Common Metals, 1975, 41: 211−224.

[48] BEHNAGH R A, GIVI M K B, AKBARI M. Mechanical properties, corrosion resistance, and microstructural changes during friction stir processing of 5083 aluminum rolled plates [J]. Materials and Manufacturing Processes, 2012, 27(6): 636−640.

[49] RAMBABU G, NAIK D B, RAO C H V, RAO K S. Optimization of friction stir welding parameters for improved corrosion resistance of AA2219 aluminum alloy joints [J]. Defence Technology, 2015, 11(4): 330−337.

[50] RASOULI S, BEHNAGH R A, DADVAND A, SALEKI-HASELGHOUBI N. Improvement in corrosion resistance of 5083 aluminum alloy via friction stir processing [J]. Proceedings of Institution of Mechanical Engineers: Part L, 2016, 230(1): 142−150.

[51] OGUOCHA I N A, ADIGUN O J, YANNACOPOULOS S. Effect of sensitization heat treatment on properties of Al−Mg alloy AA5083-H116 [J]. Journal of Material Science, 2008, 43(12): 4208−4214.

[52] HUMPHREYS F J, HATHERLY M. Recrystallization and related annealing phenomena [M]. Elsevier, 1995.

[53] LEKATOU A, SFIKAS A K, PETSA C, KARANTZALIS A E. Al−Co alloys prepared by vacuum arc melting: Correlating microstructure evolution and aqueous corrosion behavior with Co content [J]. Metals, 2016, 6(3): 46.

[54] MUDALI U K, KAUL R, NINGSHEN S, GANESH P, NATH A K, KHATAK H S, RAJ B. Influence of laser surface alloying with chromium and nickel on corrosion resistance of type 304L stainless steel [J]. Materials Science and Technology, 2006, 22(10): 1185−1192.

# 搅拌摩擦加工对 Al−$TiB_2$ 复合材料在 3.5 wt.%氯化钠溶液中腐蚀行为的影响

Ritukesh SHARMA[1], Amit Kumar SINGH[2], Amit ARORA[2], S. PATI[1], P. S. DE[1]

1. School of Minerals, Metallurgical and Materials Engineering, Indian Institute of Technology Bhubaneswar, India;

2. Materials Science and Engineering, Indian Institute of Technology Gandhinagar, India

**摘　要：**研究铸态和搅拌摩擦加工后的 Al−$TiB_2$ 基复合材料在 3.5 wt.%氯化钠溶液中的显微组织和腐蚀行为。采用 X 射线衍射、扫描电镜和电子背散射衍射技术对材料的显微组织进行表征，并采用线性/循环动电位极化、电化学阻抗谱和 ASTM−G67 测试评估材料的腐蚀行为。 结果显示，复合材料铝基体中含有亚微米级的 $TiB_2$ 颗粒，其周围围绕着块状和细小的 $Al_3Ti$ 团簇，材料表现出较低且均匀的腐蚀速率。在动电位循环测验中，没有出现正循环曲线，证明其具有抵抗点蚀的能力，这归因于 $TiB_2$ 粒子的非导电性本质和块状 $Al_3Ti$ 相的含量可控。然而，无论是搅拌摩擦加工态还是铸态复合材料都容易发生晶间腐蚀，晶界处的 $Al_3Ti$ 和 $TiB_2$ 是腐蚀的起始位点；电化学阻抗研究表明，这是由于 $Al_3Ti$ 和 $TiB_2$ 对保护氧化膜具有不利影响，且随着浸泡时间的增加，其不利影响增加。

**关键词：**搅拌摩擦加工；腐蚀行为；Al 基复合材料；电化学阻抗谱(EIS)

**(Edited by Bing YANG)**